

Revised and resubmitted to *Geophys. J. Int.*

Three-dimensional P- and S-wave velocity structure and low-frequency earthquake  
locations in the Parkfield, California region

Xiangfang Zeng<sup>1\*</sup>, Clifford H. Thurber<sup>1</sup>, David R. Shelly<sup>2</sup>, Rebecca M. Harrington<sup>3</sup>,  
Elizabeth S. Cochran<sup>4</sup>, Ninfa L. Bennington<sup>1</sup>, Dana Peterson<sup>1</sup>, Bin Guo<sup>1</sup>, and Kara  
McClement<sup>1</sup>

1. University of Wisconsin-Madison, Madison, WI, 53706
2. US Geological Survey-Menlo Park, Menlo Park, CA, 94025
3. McGill University, Montreal, Canada
4. US Geological Survey-Pasadena, Pasadena, CA, 91106

\*zengxf@geology.wisc.edu, to whom correspondence should be addressed

## Summary

To refine the 3D seismic velocity model in the greater Parkfield, California region, a new dataset including regular earthquakes, shots, quarry blasts, and low-frequency earthquakes (LFEs) was assembled. Hundreds of traces of each LFE family at two temporary arrays were stacked with time-frequency domain phase weighted stacking (tf-PWS) method to improve signal-to-noise ratio. We extend our model resolution to lower crustal depth with LFE data. Our result images not only previously identified features but also low velocity zones (LVZs) in the area around the LFEs and the lower crust beneath the southern Rinconada Fault. The former LVZ is consistent with high fluid pressure that can account for several aspects of LFE behavior. The latter LVZ is consistent with a high conductivity zone in magnetotelluric studies. A new  $V_s$  model was developed with S picks that were obtained with a new auto-picker. At shallow depth, the low  $V_s$  areas underlie the strongest shaking areas in the 2004 Parkfield earthquake. A high  $V_p/V_s$  zone in the middle crust on the northwest side of the San Andreas Fault was also revealed. We relocate LFE families and analyze the location uncertainties with the NonLinLoc and tomoDD codes. The two methods yield similar results.

**Keywords:** Tomography, Parkfield, LFE

## Introduction

The San Andreas Fault (SAF) at Parkfield and the surrounding region of central California have been the subject of intensive geophysical and geological investigation for the last few decades. One initial phase of emphasis was due to the Parkfield Prediction Experiment (PPE). Bakun and Lindh (1985) predicted a time window of  $1988 \pm 5$  years for a recurrence of the Parkfield M 6 earthquake, leading to a major, sustained geophysical monitoring effort. Although the prediction itself was not successful, the substantial knowledge resulting from the PPE played a role in the selection of the Parkfield segment of the SAF for a major fault-zone drilling project, the San Andreas Fault Observatory at Depth (SAFOD). Planning for SAFOD in turn led to renewed geological and geophysical investigations, particularly at finer scales. The occurrence of the Parkfield earthquake in September 2004, after the completion of Phase II of the SAFOD drilling, refocused some attention on the larger scale structure around Parkfield, including the modeling of strong motion and geodetic data for the 2004 earthquake.

Thurber et al. (2006) developed a regional 3D P-wave velocity model for the greater Parkfield region, and used it to relocate thousands of earthquakes and determine focal mechanisms for about 450 earthquakes. Their model has since been used to estimate 3D S-wave velocity models, using empirical relations, for locating low-frequency earthquakes (LFEs) (Shelly and Hardebeck, 2010) and determining 3D Green's functions for strong motion modeling (Gallovic et al. 2010; Sesetyan et al., 2015). Here we extend the 3D tomography work of Thurber et al. (2006) to produce a 3D S-wave velocity model and an improved P-wave velocity model by substantially increasing the number of earthquakes in the dataset, vastly enlarging the available S picks using a new automatic picker (Rawles and Thurber, 2015), and incorporating picks from stacks of LFE families computed with phase-weighted stacking (Thurber et al., 2014). The inclusion of LFE data also allows us to extend the depth of imaging to the lower crust where the LFEs occur.

## Data and Method

The starting point of our dataset is that of Thurber et al. (2006). The previous dataset includes 80,823 picks at 923 stations from 2,374 events. We extended that with data from several sources. More than 11,000 P and S picks at the Pacific Gas and Electric (PG&E) Central Coast Seismic Network were added. To better constrain S-wave structure, a new S-wave autopicker (Rawles and Thurber, 2015) was employed to pick S arrivals at Northern California Seismic Network stations as well as at the PERMIT array (Parkfield Experiment to Record Microseismicity and Tremor; Horstmann et al., 2013, 2015) deployed from May 2010 until June 2011. This picker provided 8,867 high quality S wave picks from 151 earthquakes and 81 quarry blasts (as identified in the USGS catalog) to complement existing catalog P and S picks. The locations of quarry sites were identified using Google Earth. In total 74 blasts have been assigned to four quarry sites.

Both P and S arrivals of the LFE families have been previously picked at permanent stations (Shelly and Hardebeck, 2010). Additional picks at two temporary arrays PASO (Parkfield Area Seismic Observatory; Thurber et al., 2003) and PERMIT were obtained from stacks created with the tf-PWS stacking method (Thurber et al., 2014). Since picking is affected by signal quality, the original picks of LFE data were checked by a quality control scheme based on differential time. We calculated the mean and standard deviation of differential times between event pairs, and the picks that were beyond two standard deviations were defined as outliers. We also measured differential times of LFE events using cross-correlation at PASO stations to improve precision. Finally, our LFE dataset includes 1,765 P and 2,949 S absolute arrivals from 86 LFE families and there are 11,274 P and 21,317 S catalog differential times. The regular earthquake dataset also includes 94,166 P and 37,995 S differential times from waveform cross-correlation. To improve the stability of the inversion, events with fewer than 6 picks were removed. The final dataset includes 141,234 cross-correlation differential times, 850,939 catalog differential times, and 142,550 P and 26,447 S absolute times from 4,339 events.

With the differential and absolute times, hypocenters, 3D P- and S-wave velocity structure were jointly inverted with the tomoDD algorithm (Zhang and Thurber, 2003, 2006). Our starting model is based on Thurber et al. (2006) with additional horizontal nodes at  $X = -25$  km and  $Y = -40$  km (Figure 1). The nodes in the Z direction are at 0, 2, 4, 6, 9, 12, 16, 22, and 28 km. Nodes in the Y direction were modified to -70, -50, -40, -30, -21, -15, -9, -3, 9, 15, 21, 30, 40 and 50 km. Since the  $V_p/V_s$  model also shows strong lateral heterogeneity (Zhang et al., 2009), the  $V_p/V_s$  ratios at shallow depths ( $< 10$  km) are set to be different on each side of the SAF in the upper crust of the starting model to reflect geologic differences. On the northeast side, the  $V_p/V_s$  ratio ranges from 1.9 near the surface to 1.72 at depth, whereas it ranges from 1.8 to 1.75 on the southwest side. The  $V_p/V_s$  ratio in the lower crust on both sides is computed with an empirical relationship (Brocher, 2005). There are still far fewer S than P picks, so a coarser mesh was utilized in a separate inversion in order to invert the  $V_s$  model reliably. Since the hypocenter relocation converges more slowly than inversion for velocity, we added a relocation step after each joint inversion step. The weight assigned to absolute arrivals is highest for early iterations with the weight of differential times increased in subsequent iterations. The tomoDD code utilizes both damping and smoothing. The purpose of the damping parameter is to maintain an acceptable condition number for LSQR, although it also provides some regularization in the form of damping the amplitude of model perturbations. The smoothing is specifically for regularizing the roughness of the model perturbations. The smoothing constraints and damping factors were set according to a tradeoff curve between data misfit and the norm of model (Figure S1). Both the smoothing constraints in three directions and the damping factor were kept constant during the inversion, at 20 and 45 respectively.

## Inversion Validation and Convergence

To test the quality of our results, we carried out standard checkerboard tests using the same data distribution and inversion parameters. The  $1 \times 1$  checkerboards (size of anomalies equal one grid cell) for very shallow depths ( $Z = 1, 2$  km) could be recovered near the SAFOD site. The  $V_p$  structure between 4 km and 12 km depth could be well constrained by the substantial number of earthquakes that occur in the upper crust. The  $2 \times 2$   $V_s$  checkerboards at shallow depth ( $Z = 0, 3$  km) could be recovered near the fault zones and in the coastal area. In most areas, the  $V_s$  pattern can be recognized down to 21 km. As a result of the LFE data, the deepest checkers near the SAF fault zone could be recovered as well (Figure 2).

For the real data after 12 iterations, the root-mean-square (RMS) of both catalog and cross-correlation times were substantially reduced (Figure 3). The RMS of catalog times decreased about 57% (from 229 ms to 99 ms) whereas the RMS of cross-correlation times was reduced by about 66% (from 83.5 ms to 28.2 ms).

## Inversion Result: $V_p$ and $V_s$ model

The velocity contrast across the SAF has been reported in previous 3D tomography model and reflection profiles (Figures 4 and 5, e.g. Michelini and McEvilly, 1991; Eberhart-Phillips and Michael, 1993; Thurber et al., 2006; Bleibinhaus et al., 2007; Roux, 2009). The southwest side is generally faster, corresponding to the granitic rocks of the Salinian block, whereas the northeast side with lower velocities consists mainly of the Great Valley sequence and Franciscan assemblage rocks. In the northern segment, the fault zone is dominated by a simple contrast across the fault (Figure 4; Y nodes from -3 to 30 km) that extends down to  $\sim 15$  km depth in the  $V_p$  model. Due to resolution limitations, the  $V_s$  contrast across the SAF is smoother than that of the  $V_p$  model. A middle crust low velocity zone dipping to the southwest is clearly imaged in sections  $Y = 9$  and 3 km of the  $V_s$  model (Figure 5). In the southern segment, the  $V_p$  and  $V_s$  model patterns across the SAF are similar to each other.

We observed no clear velocity contrast across the Rinconada Fault ( $X \sim -40$  km; Figure 4 and 5). Based on the velocities observed, the material on both sides of the Rinconada Fault likely belongs to the Salinian block. Previous large- and small- scale models suggested that there is no significant lateral variation in the upper crust near the Rinconada Fault (Lin et al., 2010; Hardebeck, 2010).

A clear velocity contrast between the sedimentary rocks and underlying basement in the Coalinga area is obvious in sections from  $Y = -3$  km to 50 km (down to about 10 km, Figure 4). In the  $V_p$  model, the high velocity body (HVB,  $V_p \sim 6.0$  km/s) on the southwest side is clearly visible from 12 km to 4 km depth and the southern part ( $Y = 9$  km, Figure 4) is more sharply defined than the northern part. This feature has been

interpreted as a fragment of the Coast Range Ophiolite sandwiched between the Franciscan and Great Valley sequence (Eberhart-Phillips, 1990). Since the  $V_s$  increase is much smaller in this HVB (Figure 5), the fault plane shows a strong contrast in  $V_p/V_s$ , which is consistent with expectations based on rock types (Brocher, 2005). The hanging wall appears as a LVZ ( $Z = 9$  km, Figure 6b) that is likely an additional Great Valley sequence layer over basement. Although the main fault plane dips to the northeast, there is another potential southwest-dipping fault plane associated with a small earthquake cluster (dashed lines in Figure 4).

A small HVB on the southwest side of the SAF beneath Middle Mountain is also revealed at 4 km depth in the  $V_p$  model ( $Y \sim -20$  to 0 km, Figure 6a; Eberhart-Phillips and Michael, 1993). In the  $V_s$  model, this HVB is present between 3 and 6 km depth, but appears somewhat smaller. This HVB is consistent with the existence of an elliptical magnetic and high gravity zone that was interpreted as magnetic granitic rocks over non-magnetic Salinian basement (McPhee et al., 2004).

A significant high velocity body on the northeast side of the SAF is imaged near Gold Hill that extends down to 10 km in the  $V_p$  model ( $X \sim 1$  to 10 km, Figure 6b). This HVB was previously revealed in first-P-arrival tomography (Eberhart-Phillips and Michael, 1993; Thurber et al., 2006) and also confirmed with a dataset including secondary P arrivals (Bennington et al., 2013). This region is marked by a 10 mGal isostatic residual gravity anomaly, indicating higher density rock (Snyder and Carr, 1984). The velocity is even higher than that on the southwest side of the SAF, and it has been interpreted as greenstones and mafic rocks of the Permanente Terrain (Eberhart-Phillips and Michael, 1993; Thurber et al., 2006). The area corresponds approximately to the main rupture patch of the 2004 Parkfield mainshock. The high velocities on both sides of the fault suggest greater fault strength and the ability to store more strain energy to eventually release as a larger earthquake (Eberhart-Phillips and Michael, 1993; Thurber et al., 2006).

At greater depth ( $Z = 9$  km), this HVB connects with an along-strike linear HVB ( $Y = -21$  to  $-50$  km) that is about 2 km away from the SAF. The low velocity along the SAF trace may due to a broad damage zone with distributed parallel faults instead of a single fault in the upper crust, consistent with magnetic and gravity observations (Thurber et al., 2006).

Several other low velocity features are revealed in our results. Dimensions of the large low velocity basin-like feature on the northeast side of the SAF at 4 km depth are similar to previous results ( $X = 2$  to 10 km,  $Y = 3$  to 21 km; Eberhart-Phillips and Michael, 1993) with about a 10% decrease. This LVZ is slightly larger and stronger in the  $V_s$  model. In gravity and aeromagnetic maps, this region is shown as an elliptical magnetic high and gravity low interpreted as serpentinite in Franciscan rocks (McPhee et al., 2004). A similar low velocity serpentinite was reported in a seismic-refraction profile

in the Santa Clara Valley (Mooney and Colburn, 1985). This low velocity body also underlies the area of strongest shaking during the 2004 Parkfield mainshock (Bakun et al., 2005). Besides the amplification effect of rupture directivity, the basin-like structure likely amplifies and extends the duration of ground motion (Gallovcic et al., 2010). Two other areas of low velocity at shallow depth are imaged in our Vs model (Figure 6d). The southeast one ( $X = -10$  km,  $Y = -21$  km) is close to the epicenter of the 2004 Parkfield earthquake. The other one ( $X = 2$  km,  $Y = -30$  to  $-50$  km) is on the northeast side of the SAF near Cholame Valley. Both zones also underlie strong ground shaking during the 2004 Parkfield mainshock (Bakun et al., 2005; Shakal et al., 2006). The GH3W station in the southeast LVZ also recorded large ground motions during the 1983 Coalinga earthquake (Shakal et al., 2006). This consistency supports the influence of heterogeneity of shallow structure on ground motion (Gallovcic et al., 2010).

A lower crustal P-wave LVZ was imaged in the section  $Y = -40$  km (Figure 4).  $V_p$  is reduced by about 0.5 km/s from the surrounding rock, but the LVZ is not clear in the Vs model. This LVZ is about 20 km by 20 km at 16 to 22 km depth and it may be in contact with the SAF. We note that the checkerboard pattern in this cross section was recovered adequately suggesting we do have sufficient resolution to image these features (Figure 7). We also designed a restoration test to confirm our result. The test consists of a synthetic dataset that was generated from our final model. We then obtained an output model from an inversion of the synthetic dataset using the same parameters. The LVZ was recovered by the inversion (Figure 8). With reflection and refraction data, Trehu and Wheeler (1987) reported a LVZ (LVZ in Figure 4) in the lower crust between the SAF and Rinconada Fault using reflection and refraction data collected along an active source profile located close to the  $Y = -40$  km section. The depths of the two LVZs are comparable but our result is slightly east of that reported in Trehu and Wheeler (1987). In Trehu and Wheeler (1987), the LVZ location is consistent with the western portion of a strong reflectivity zone (REF in Figure 4), whereas the LVZ in our  $V_p$  model covers the eastern portion of the strong reflectivity zone. Therefore the slight difference could be due to sampling differences. The LVZ was sampled by deep reflected rays in Trehu and Wheeler (1987), which only sampled the western portion, whereas LFE data contributes most deep rays in the eastern portion in our inversion. Furthermore an along strike high conductivity zone (HCZ) in the lower crust and upper-most mantle was imaged in a magnetotelluric inversion (HCZ in Figure 4; Becken et al., 2011) that is consistent with the presence of a LVZ. They suggest that the lower crust is fluid rich and has been weakened. The different locations for our LVZ and the high conductivity zone could again be due to different spatial sampling.

There are two other LVZs in the deep crust ( $Z = 16$  km, Figure 6c). One LVZ is close to the SAF to the north of Parkfield ( $X = -8$  to  $3$  km,  $Y = 15$  and  $31$  km). Another is to the east of Cholame ( $X = 17$  km) where it is separated from the SAF by a narrow HVB.



These LVZs in the lower crust may correspond to a low velocity layer in the receiver function study of Ozacar and Zandt (2009) that is interpreted to represent a layer of metasedimentary rocks.

### **Inversion Result: LFE locations**

The locations of NVT have been studied with different datasets and location methods. In one approach, differential arrival times between station pairs measured with envelope cross-correlation were used with a grid search and station-pair double-difference location methods (Nadeau and Dolenc, 2005; Zhang et al., 2010). In a different approach, several small aperture arrays near Parkfield and Cholame provided high quality records that were used with array techniques to estimate the location of individual tremor events (Fletcher and Baker, 2010; Ryberg et al., 2010). In these studies, the location of NVT is generally widely scattered. In contrast to the generally emergent character of NVT wavetrains, LFEs during tremor provide much clearer onsets of body waves, especially when LFE events with similar waveforms are stacked to improve signal quality (Shelly and Hardebeck, 2010). Using a prior 3D Vs model to determine 88 LFE family locations, the results of the latter study suggest that most LFEs are concentrated close to the SAF at depths from 18 to 28 km, much shallower and more concentrated than the NVT results (e.g. Nadeau and Dolenc, 2005), in between the seismogenic layer and Moho discontinuity. However, the location difference between LFEs and NVT is still controversial (Shelly et al., 2007; Guilhem and Nadeau, 2012). Picks at temporary stations that are close to the SAF likely provide a tighter constraint on depth. Event-pair differential times can also be helpful to improve location precision (Figures 9 and 10).

The RMS misfits of most LFE families are less than 0.1 s and both horizontal and vertical uncertainties are less than 1 km (Figure 9). Since the accuracy of the standard error computed with the conjugate gradients method (LSQR, Paige and Saunders, 1982) may be underestimated (Waldhauser and Ellsworth, 2000), we also applied another relocation with singular value decomposition (SVD) to access the uncertainties and obtained a similar result. The uncertainties of LFE families in the northern segment are much larger than the southern ones. A grid search location method with oct-tree sampling algorithm (Non-Linear Location, NonLinLoc; Lomax et al., 2009) was also utilized to evaluate the location results. The travel-time tables were calculated with our final velocity model using the finite difference algorithm. Although the NonLinLoc results are independent of the initial location, the final locations are generally consistent with our result. This method also provides probability distribution functions of location that are a reliable estimate of uncertainties. As Figure 10 shows, the average length of the semi-major-axis of the 68% confidence ellipsoid is about 3 km. We note that the uncertainties obtained from NonLinLoc relate to the error of absolute location whereas the ones from tomoDD reflect relative location uncertainties. The location uncertainties



for the southern LFEs are smaller than the northern ones due to more frequent occurrence, higher amplitude, and better station distribution, although the RMS residuals are larger.

The overall pattern of our LFE relocations is consistent with the previous result of Shelly and Hardebeck (2010; Figure 9) although we used whole dataset instead of three overlapping sets of stations. The most obvious differences in locations are found for the LFEs that occur near the 2004 mainshock ( $Y \sim -25$  to  $-10$  km) and at the north end of the study area ( $Y \sim 30$ - $50$  km). The NonLinLoc and tomoDD locations suggest that five LFEs occur below the surface trace of the southwest fault zone, which agrees with microseismicity locations in the upper crust (Thurber et al., 2006).

The portion of the San Andreas Fault that lies northwest of Parkfield is hypothesized to be much weaker due to the presence of fluid (Becken et al., 2011) and the LFE amplitudes are reported to be about 50% lower than for ones beneath Cholame (Shelly and Hardebeck, 2010). The lower amplitudes and rate northwest of Parkfield also limited the usable traces for stacking leading to reduced signal quality. In the NonLinLoc result, the LFEs in the northern segment ( $Y \sim 30 - 50$  km) show a clear southwestward shift compared to the original locations (Figure 11). A similar shift is observed in an evenly spaced grid search result, however this shift does not appear in the tomoDD result (Figure 9, Table S1). There are some possible causes for such a deviation between the tomoDD and grid search methods. One possibility is that tomoDD uses differential times to refine the location while the grid search methods use direct arrival times. To test this, the relative weight of differential times was significantly reduced, but we observed no systematic change in the results. We also used the NonLinLoc results as the initial locations in the tomoDD code to test if tomoDD falls into local misfit minima, but again the final tomoDD relocations remained essentially unchanged. We also investigated whether residual re-weighting may influence the final relocations. The re-weighting based on residual is included in tomoDD to remove outliers that may exert a large influence on the least squares fit. We observe in the tomoDD results without residual re-weighting a southwestward shift for the northern LFEs. Thus the weaker LFEs in the northern segment make it more difficult to identify arrivals accurately causing significant outliers that can in turn bias the locations. The quality of picks of LFEs in the southern segment is much higher leading to more consistent location results with the different methods. Waveform stacks over a longer time periods are needed to improve the locations along the segment of the San Andreas Fault northwest of Parkfield.

The LFE families beneath Cholame Valley are concentrated in about a 4 km wide zone, about 3 km southwest of the surface trace of the SAF (Figure 9). There are some LFE families on the northeast side of the SAF separated from the clusters beneath the SAF. Shelly (2015) proposed that such isolated LFEs may occur along the upper interface of the Monterey microplate, a remnant of the subducted Farallon plate that might deflect the SAF eastward in the mantle.

The depths of LFEs are consistent with that of a high resistivity zone, interpreted to be under high fluid pressure and facilitating brittle failure (Becken et al., 2011). There is an obvious LFE gap beneath the 2004 Parkfield earthquake rupture patch (Shelly and Hardebeck, 2010). A low resistivity fluid channel that connects the high conductivity zone beneath the Rinconada Fault and the SAF was imaged in a 3D magnetotelluric inversion (Tietze and Ritter, 2013). They hypothesized that a fluid-filled porosity network causes fault weakening, so brittle failure as LFEs cannot occur. An alternative hypothesis is that weak signals of undetected LFEs may be hidden by background noise (Shelly and Hardebeck, 2010).

### **Conclusions and Future work**

New earthquake and LFE data are employed to update an existing 3D Vp model and develop a new Vs model for the Parkfield region using double-difference tomography. A deep LVZ between the SAF and Rinconada Fault was imaged in our inversion that is close to a high conductivity zone. Two other smaller LVZs in the lower crust are also present in the new model. Such LVZs may reflect fragments of metasedimentary rocks in the Parkfield region. The Vs model reveals several LVZs at shallow depth that is consistent with area of high amplitude strong motions from the 2004 Parkfield earthquake. With the new model, we also relocated 84 LFE families. The relocation result is generally consistent with the previous study of Shelly and Hardebeck (2010); the location uncertainty of most LFE families is less than 5 km.

Although more S picks were used in our inversion, the resolution of our Vs model is still not as good as the Vp model. An alternative choice is ambient noise tomography (ANT). ANT has been utilized in southern California (Shapiro et al., 2005; Zigone et al., 2015), a small region near Parkfield (Roux, 2009) and many other areas. The velocity contrast across the SAF was imaged by the previous ANT study (Roux, 2009), and a new body-wave and surface-wave joint inversion method applied to the same area revealed further small-scale features (Zhang et al., 2014). Application of ANT and joint tomography may be the keys to further improving our knowledge of the 3D Vs structure in the Parkfield region.

### **Acknowledgments**

Research was supported in part by the USGS, Department of the Interior, under USGS Award Number G14AP00056 to the University of Wisconsin-Madison. The views and conclusions contained in this document are those of the authors and should not be interpreted as necessarily representing the official policies, either expressed or implied, of the U.S. Government. This research was also supported in part by the Southern California Earthquake Center (SCEC). SCEC is funded by NSF Cooperative Agreement

EAR-0106924 and USGS Cooperative Agreement 02HQAG0008. Waveform data for this study accessed through the Northern California Earthquake Data Center (NCEDC, doi:10.7932/NCEDC). All figures were plotted with the Generic Mapping Tools (Wessel and Smith, 1991).

## References

- Bakun, W. H. and Lindh, A. G. (1985). The Parkfield, California, earthquake prediction experiment, *Science*, 229(4714), 619-624.
- Bakun, W. H., Aagaard, B., Dost, B., Ellsworth, W. L., Hardebeck, J. L., Harris, R. A., Ji, C., Johnston, J. S., Langbein, J., Lienkaemper, J. J., Michael, A. J., Murray, J. R., Nadeau, R. M., Reasenberg, P. A., Reichle, M. S., Roeloffs, E. A., Shakal, A., Simpson, R. W., and Waldhauser, F. (2005). Implications for prediction and hazard assessment from the 2004 Parkfield earthquake. *Nature*, 437(7061), 969-974.
- Becken, M., Ritter, O., Bedrosian, P. A., and Weckmann, U. (2011). Correlation between deep fluids, tremor and creep along the central San Andreas fault. *Nature*, 480(7375), 87-90.
- Bennington, N. L., Thurber, C., Peng, Z., Zhang, H., and Zhao, P. (2013). Incorporating fault zone head wave and direct wave secondary arrival times into seismic tomography: Application at Parkfield, California. *J. Geophys. Res.*, 118(3), 1008-1014.
- Bleibinhaus, F., Hole, J. A., Ryberg, T., and Fuis, G. S. (2007). Structure of the California Coast Ranges and San Andreas Fault at SAFOD from seismic waveform inversion and reflection imaging. *J. Geophys. Res.*, 112, B06315.
- Brocher, T. (2005). Empirical relations between elastic wavespeeds and density in the Earth's crust. *Bull. Seismol. Soc. Am.*, 95(6), 2081-2092.
- Eberhart-Phillips, D. (1990). Three-dimensional P and S velocity structure in the Coalinga Region, California. *J. Geophys. Res.*, 95(B10), 15343-15363.
- Eberhart-Phillips, D., and Michael, A. J. (1993). Three-dimensional velocity structure, seismicity, and fault structure in the Parkfield region, central California. *J. Geophys. Res.*, 98(B9), 15737-15758.
- Fletcher, J. B., and Baker, L. M. (2010). Analysis of nonvolcanic tremor on the San Andreas fault near Parkfield, CA using US Geological Survey Parkfield Seismic Array. *J. Geophys. Res.*, 115, B10305.
- Gallovic, F., Kaser, M., Burjanek, J. and Papaioannou C. (2010). Three-dimensional modeling of near-fault ground motions with nonplanar rupture models and topography: case of the 2004 Parkfield earthquake. *J. Geophys. Res.*, 115, B03308.
- Guilhem, A., and Nadeau, R. M. (2012). Episodic tremors and deep slow-slip events in Central California. *Earth and Planetary Science Letters*, 357, 1-10.
- Hardebeck, J. (2010). Seismotectonics and fault structure of the California central coast. *Bull. Seismol. Soc. Am.*, 100(3), 1031-1050.
- Horstmann, T., Harrington, R. M., and Cochran, E. S. (2013). Semiautomated tremor detection using a combined cross-correlation and neural network approach. *J.*

- Geophys. Res., 118(9), 4827-4846.
- Horstmann, T., Harrington, R. M. and Cochran, E. S. (2015). Using a modified time-reverse-imaging technique to locate low-frequency earthquakes on the San Andreas fault near Cholame, California, *Geophys. J. Int.*, 203(2), 1207-1226.
- Lin, G., Thurber, C. H., Zhang, H., Hauksson, E., Shearer, P. M., Waldhauser, F., Brocher, T. M., and Hardebeck, J. (2010). A California statewide three-dimensional seismic velocity model from both absolute and differential times. *Bull. Seismol. Soc. Am.*, 100(1), 225-240.
- Liu, Y., Zhang, H., Thurber, C., and Roecker, S. (2008). Shear wave anisotropy in the crust around the San Andreas fault near Parkfield: spatial and temporal analysis. *Geophys. J. Int.*, 172(3), 957-970.
- Lomax, A., Michelini A., and Curtis A. (2009). Earthquake location, direct, global-search methods, in *Encyclopedia of Complexity and System Science*, Part 5, Meyers, R. A. (ed.), Springer, New York, pp. 2449-2473.
- McPhee, D. K., Jachens, R. C., and Wentworth, C. M. (2004). Crustal structure across the San Andreas Fault at the SAFOD site from potential field and geologic studies. *Geophys. Res. Lett.*, 31, L12S03.
- Michelini, A., and McEvilly, T. V. (1991). Seismological studies at Parkfield, I simultaneous inversion for velocity structure and hypocenters using cubic B-splines parameterization. *Bull. Seismol. Soc. Am.*, 81, 524-522.
- Mooney, W., and Colburn, R. (1985). A seismic-refraction profile across the San Andreas, Sargent, and Calaveras faults, west-central California. *Bull. Seismol. Soc. Am.*, 75(1), 175-191.
- Nadeau, R. M., and Dolenc, D. (2005). Nonvolcanic tremors deep beneath the San Andreas Fault. *Science*, 307(5708), 389-389.
- Ozacar, A. A., and Zandt, G. (2009). Crustal structure and seismic anisotropy near the San Andreas Fault at Parkfield, California. *Geophys. J. Int.*, 178(2), 1098-1104.
- Paige, C. C. and Saunders, M. A. (1983). LSQR: Sparse linear equations and least squares problems. *ACM Transactions on Mathematical Software*, 8(2), 195-209.
- Rawles C., and Thurber C. (2015). A nonparameteric method for automatic determination of P-wave and S-wave arrival times: application to local microearthquakes. *Geophysical Journal International*, 202(2), 1164-1179.
- Roux, P. (2009). Passive seismic imaging with directive ambient noise: application to surface waves and the San Andreas Fault in Parkfield, CA. *Geophys. J. Int.*, 179(1), 367-373.
- Ryberg, T., Haberland, C., Fuis, G. S., Ellsworth, W. L., and Shelly, D. R. (2010). Locating non-volcanic tremor along the San Andreas Fault using a multiple array source imaging technique. *Geophys. J. Int.*, 183(3), 1485-1500.
- Sesetyan, K., Cakti, E., and Madariaga, R. (2015). Engineering implications of source

- parameters and 3D wave propagation modeling for the 2004 Parkfield, California, earthquake. *Bull. Seismol. Soc. Am.*, 105(3), 1739-1755.
- Shakal, A., Haddadi, H., Graizer, V., Lin, K. and Huang M. (2006). Some key features of the strong-motion data from the M6.0 Parkfield, California, earthquake of 28 September 2004. *Bull. Seismol. Soc. Am.*, 96(4b), S90-S118.
- Shapiro, N. M., Campillo, M., Stehly, L., and Ritzwoller, M. H. (2005). High-resolution surface-wave tomography from ambient seismic noise. *Science*, 307(5715), 1615-1618.
- Shelly, D. R. (2015). Complexity of the deep San Andreas Fault zone defined by cascading tremor. *Nature Geoscience*, 8(2), 145-151.
- Shelly, D. R., and Hardebeck, J. L. (2010). Precise tremor source locations and amplitude variations along the lower-crustal central San Andreas Fault. *Geophys. Res. Lett.*, 37, L14301.
- Shelly, D. R., and Johnson, K. M. (2011). Tremor reveals stress shadowing, deep postseismic creep, and depth-dependent slip recurrence on the lower-crustal San Andreas fault near Parkfield. *Geophys. Res. Lett.*, 38(13), L13312.
- Snyder, D. B., and Carr, W. J. (1984). Interpretation of gravity data in a complex volcano-tectonic setting, southwestern Nevada. *J. Geophys. Res.*, 89(B12), 10193-10206.
- Tietze, K., and Ritter, O. (2013). Three-dimensional magnetotelluric inversion in practice—the electrical conductivity structure of the San Andreas Fault in Central California. *Geophys. J. Int.*, 195(1), 130-147.
- Thurber, C. H., Roecker, K., Gold, M., Powell, L. and Rittger, K. (2003). Earthquake locations and three-dimensional fault zone structure along the creeping section of the San Andreas fault near Parkfield, CA: Preparing for SAFOD. *Geophys. Res. Lett.*, 30(3), 1112.
- Thurber, C. H., Zeng, X., Thomas, A. M., and Audet, P. (2014). Phase-weighted stacking applied to low-frequency earthquakes. *Bull. Seismol. Soc. Am.*, 104(5), 2567-2572.
- Thurber, C., Zhang, H., Brocher, T., and Langenheim, V. (2009). Regional three-dimensional seismic velocity model of the crust and uppermost mantle of northern California. *J. Geophys. Res.*, 114, B01304.
- Thurber, C., Zhang, H., Waldhauser, F., Hardebeck, J., Michael, A., and Eberhart-Phillips, D. (2006). Three-dimensional compressional wavespeed model, earthquake relocations, and focal mechanisms for the Parkfield, California, region. *Bull. Seismol. Soc. Am.*, 96(4B), S38-S49.
- Trehu, A. M., and Wheeler, W. H. (1987). Possible evidence for subducted sedimentary materials beneath central California. *Geology*, 15(3), 254-258.
- Unsworth, M., and Bedrosian, P. A. (2004). Electrical resistivity structure at the SAFOD site from magnetotelluric exploration. *Geophys. Res. Lett.*, 31, L12S05.

- Waldhauser, F. and Ellsworth, W. L. (2000) A double-difference earthquake location algorithm: method and application to the northern Hayward fault, California. *Bull. Seismol. Soc. Am.*, 90(6), 1353-1368.
- Wessel, P., and Smith, W. H. (1991). Free software helps map and display data. *Eos, Transactions American Geophysical Union*, 72(41), 441-446.
- Zeng X., Thurber, C., Shelly, D., Bennington, N., Cochran, E. and Harrington, R. (2014) 3D P and S wave velocity structure and tremor locations in the Parkfield region. Abstract S23CA-4545 presented at 2014 Fall Meeting, AGU, San Francisco, Calif., 15-19 Dec.
- Zhang, H., Maceira, M., Roux, P., and Thurber, C. (2014). Joint inversion of body-wave arrival times and surface-wave dispersion for three-dimensional seismic structure around SAFOD. *Pure and Applied Geophysics*, 171,3013-3022.
- Zhang, H., Nadeau, R. M., and Toksoz, M. N. (2010). Locating nonvolcanic tremors beneath the San Andreas fault using a station-pair double-difference location method. *Geophys. Res. Lett.*, 37(13), L13304.
- Zhang, H., and Thurber, C. H. (2003). Double-difference tomography: The method and its application to the Hayward fault, California. *Bull. Seismol. Soc. Am.*, 93(5), 1875-1889.
- Zhang, H., and Thurber, C. (2006). Development and applications of double-difference seismic tomography. *Pure and Applied Geophysics*, 163(2-3), 373-403.
- Zhang, H., Thurber, C., and Bedrosian, P. (2009). Joint inversion for  $V_p$ ,  $V_s$ , and  $V_p/V_s$  at SAFOD, Parkfield, California. *Geochemistry, Geophysics, Geosystems*, 10, Q11002.
- Zigone, D., Ben-Zion, Y., Campillo, M., and Roux P. (2015) Seismic tomography of the Southern California plate boundary region from noise-based Rayleigh and Love waves. *Pure and Applied Geophysics*, 172(5), 1007-1032.



## Figures

Figure 1. Map of study area showing events (diamonds, squares, solid circles), two temporary arrays (open triangles) and inversion grid (crosses). Shots, blasts earthquakes and LFEs are denoted by green, red, black, and pink symbols, respectively. Blue triangles denote stations of two temporary arrays. The yellow box denotes location of the magnified insert.

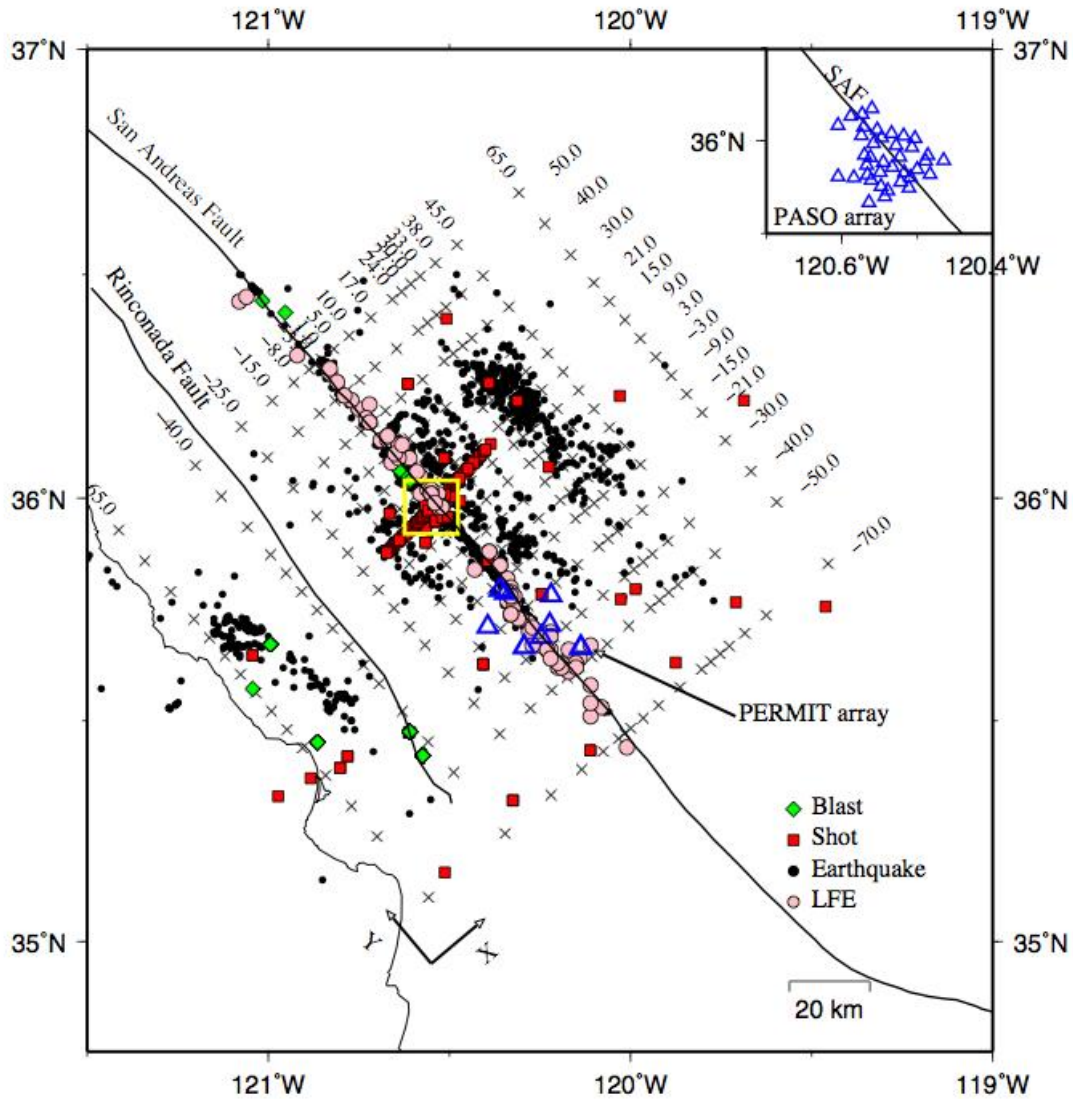


Figure 2.  $2 \times 2$  checkerboard test result for the coarser mesh for the Vs model at 21 km depth. (a) Input model; (b) Output model. The red circles indicate events.

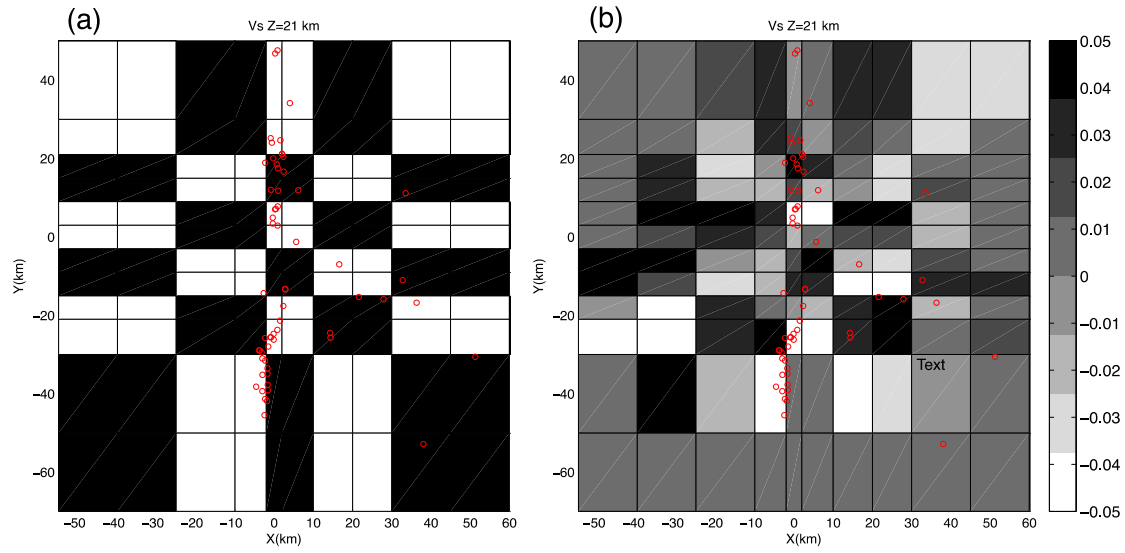


Figure 3. Travel-time residuals before (gray) and after (red) inversion.

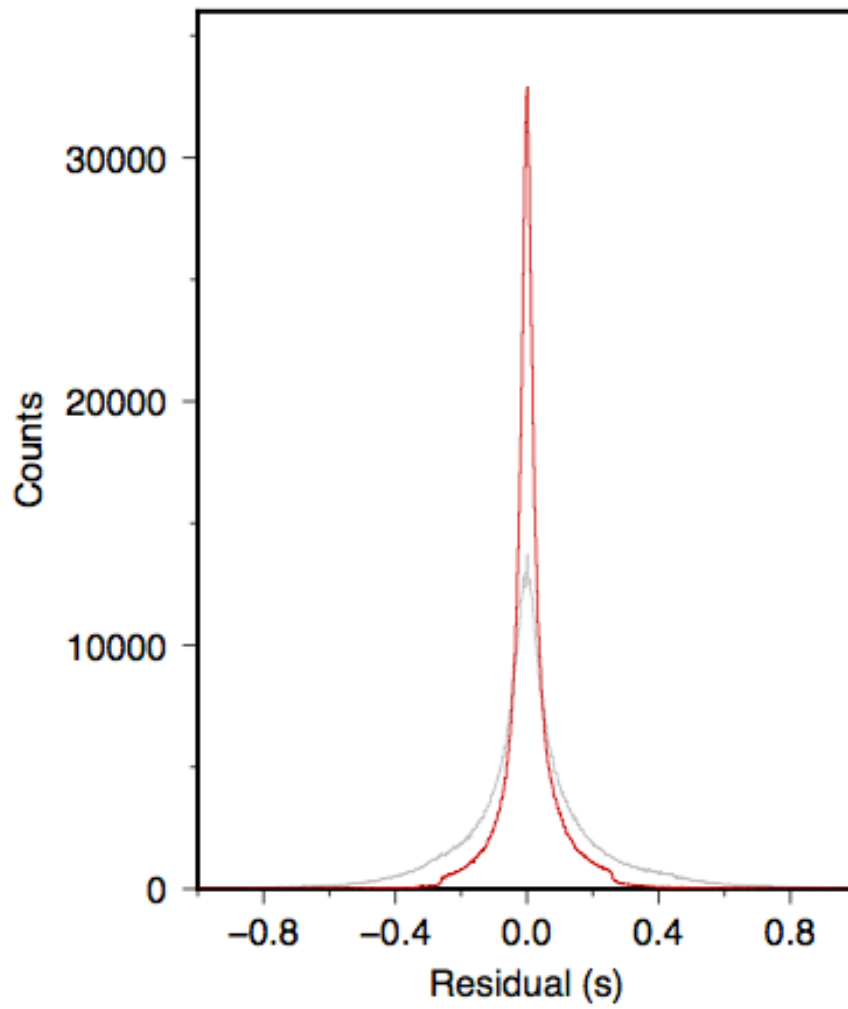
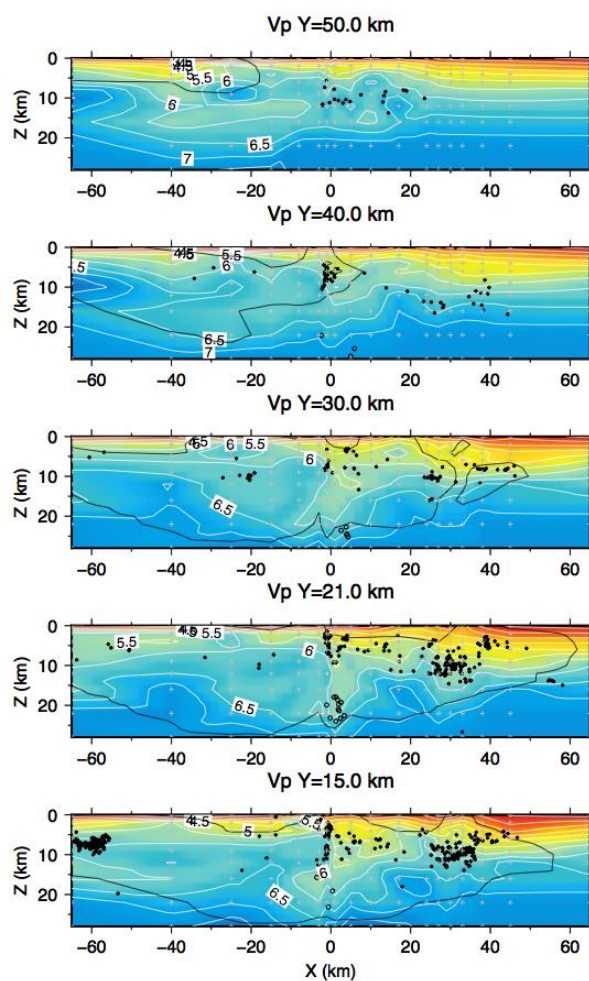


Figure 4. Cross-sections of 3D Vp model. Earthquakes (solid) and LFE families (open) are shown in black circles. The thin black contours show the limits of the region where the model is well resolved ( $DWS > 1000.0$ ). Two potential fault planes in the Coalinga region are shown in dashed lines in  $Y = 9$  km cross-section. The LVZ (black; Trehu and Wheeler, 1987), the strong reflectivity zone (pink; Trehu and Wheeler, 1987), and HCZ (red; Becken et al., 2011) in previous results are shown in solid lines in  $Y = -40$  km cross-section. Vp in km/s.



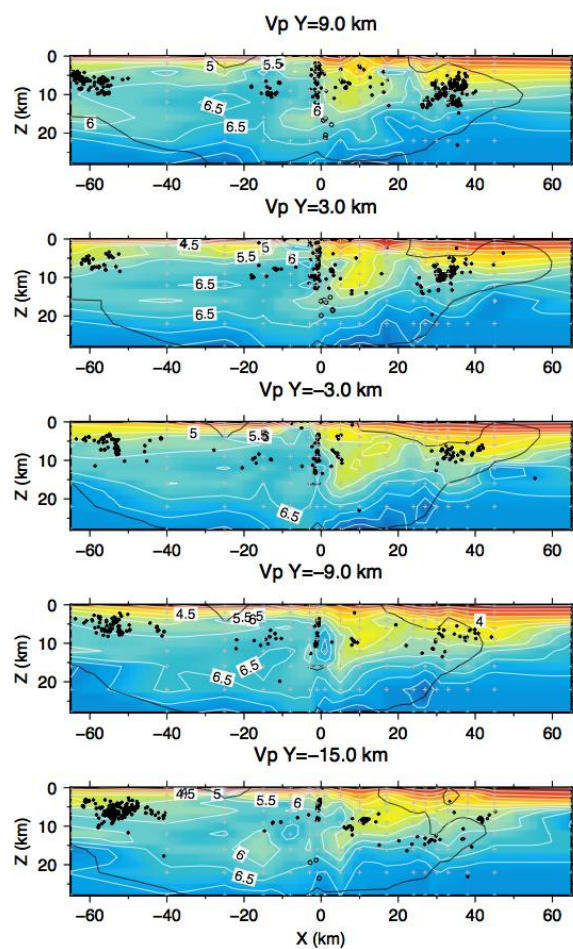


Figure 4 (continued)

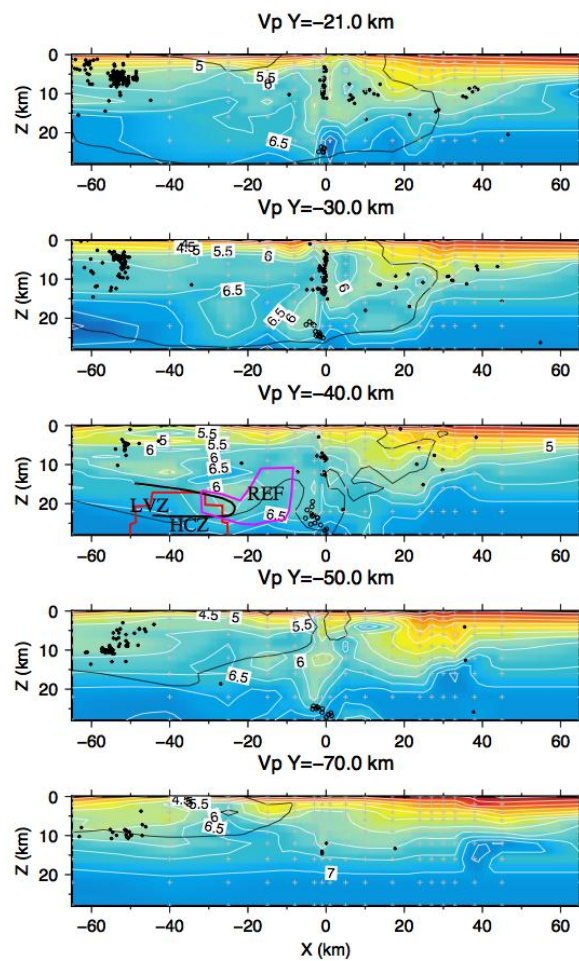
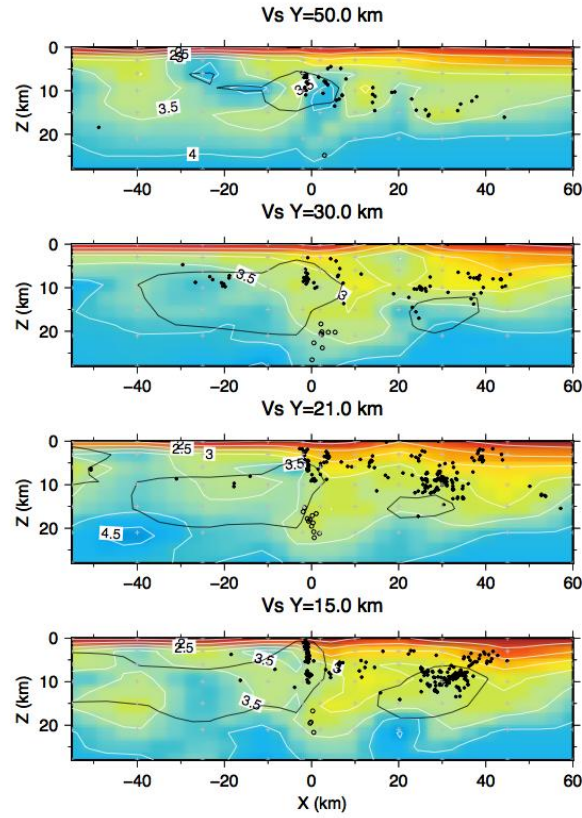


Figure 4 (continued)

Figure 5. Cross-sections of 3D  $V_s$  model. Earthquakes (solid) and LFE families (open) are shown in black circles. The thin black contours show the limits of the region where the model is resolved ( $DWS > 250.0$ ). Since a coarser mesh was adopted for determining the  $V_s$  model, the event locations are different than the ones in Figure 4.  $V_s$  in km/s.





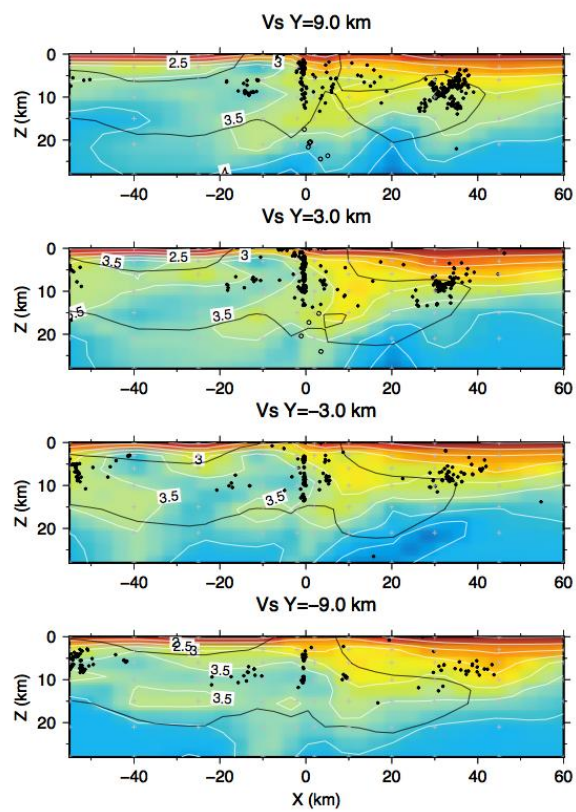


Figure 5 (continued)

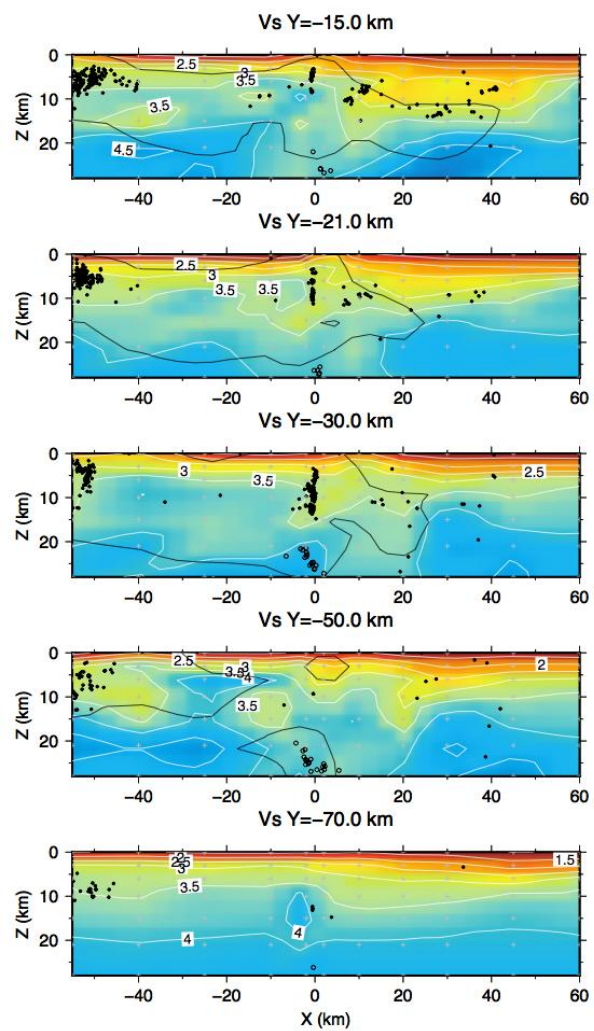


Figure 5 (continued)

Figure 6. Map views of the  $V_p$  and  $V_s$  model ( $V_p$  at  $Z = 4$  km, 9 km, 16 km,  $V_s$  at  $Z = 3$  km). The surface traces of the SAF and Rinconada Fault are shown in white line whereas black dots indicate events at depth. Local features: MM, Middle Mountain; GH: Gold Hills; CV: Cholame Valley and Coalinga: Coalinga area. Velocity in km/s.

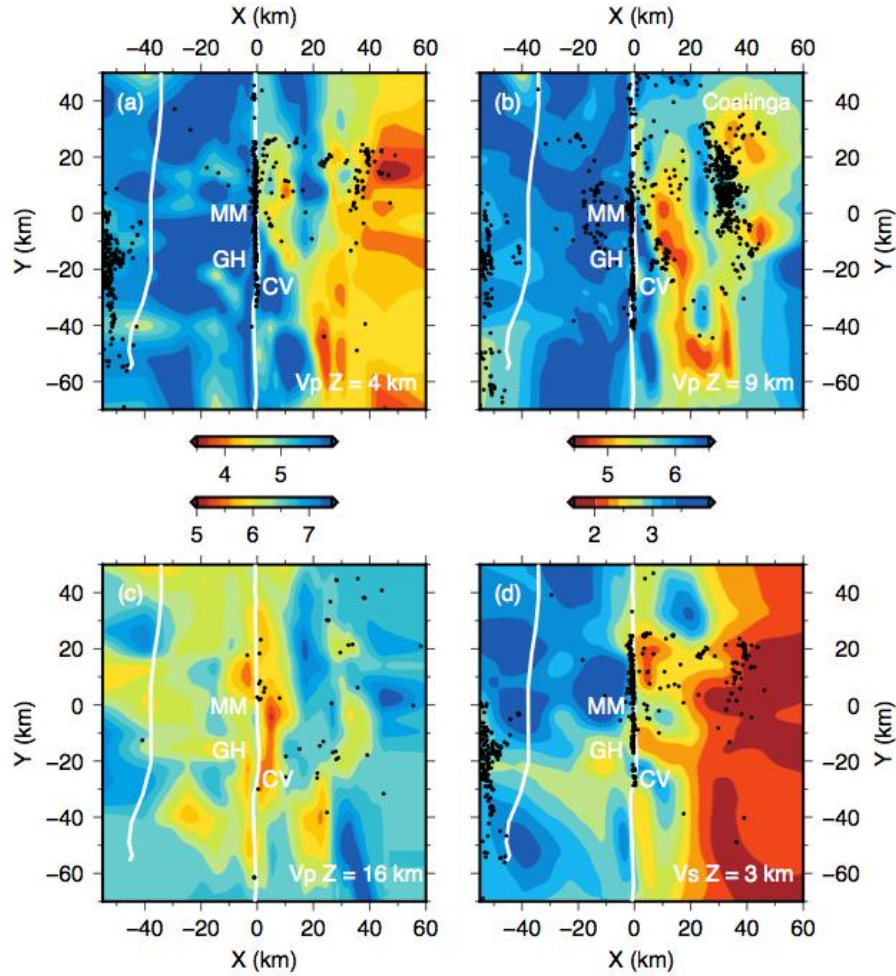


Figure 7.  $2 \times 2$  checkerboard test result for the  $V_p$  model at  $Y = -40$  km. The red dots indicate events.

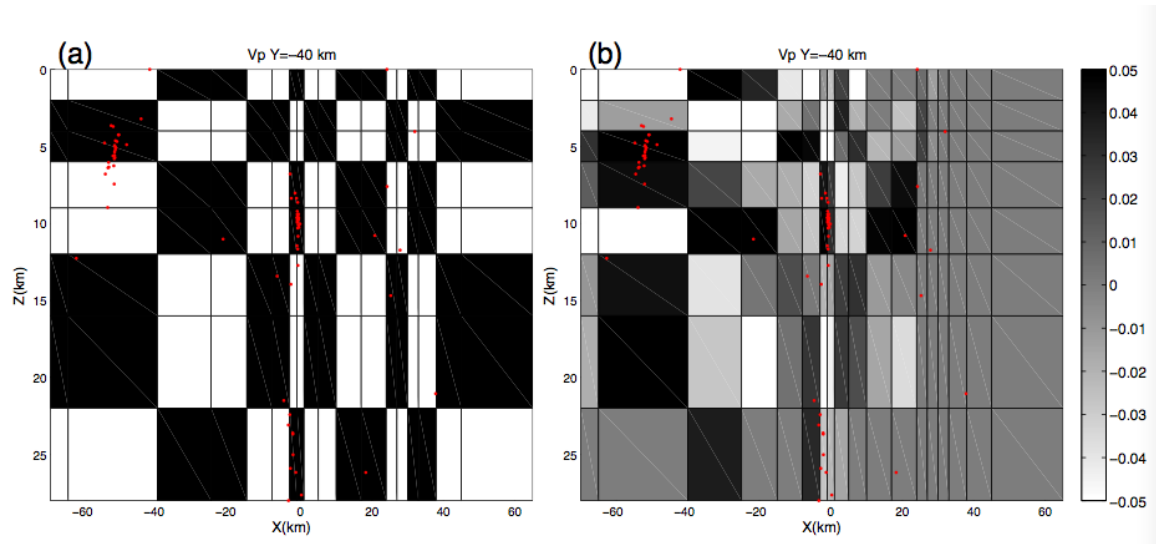


Figure 8. Cross section at  $Y = -40$  km of the output model for the restoration test. The black dots indicate events.

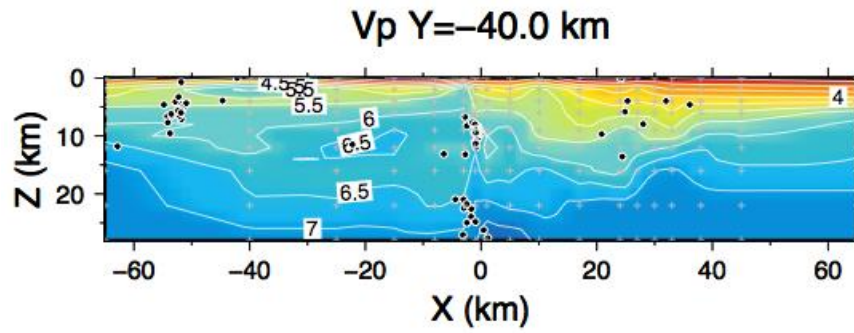


Figure 9. Maps and cross-sections showing locations of LFE familie (red circles). The hypocenters of the 1966 and 2004 Parkfield earthquakes are shown in white and red stars, respectively. The black dots indicate regular earthquakes.

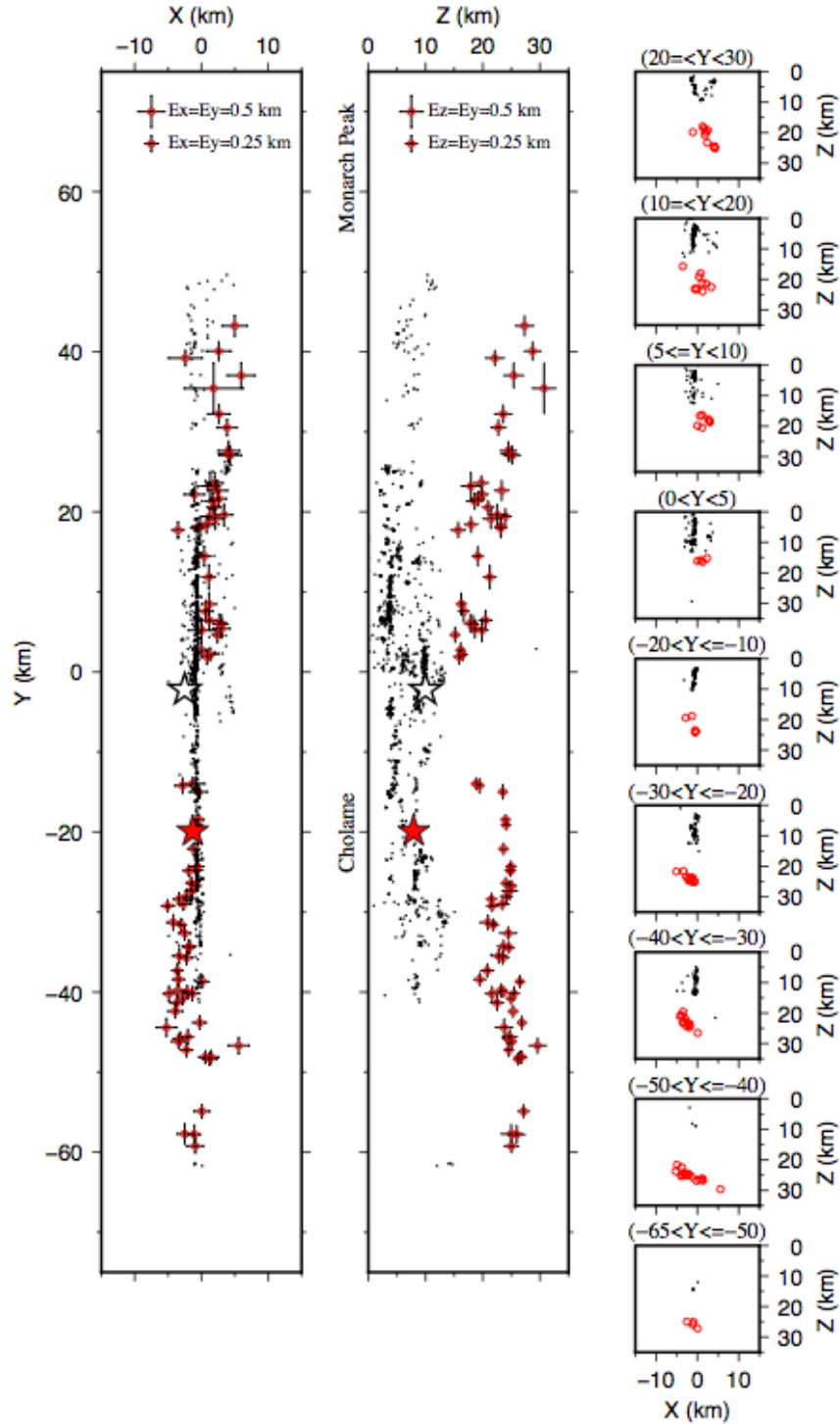


Figure 10. LFE family location results using NonLinLoc code. The 68% confidence ellipsoids are indicated with gray lines. The blue stars denote maximum-likelihood hypocenters whereas the red dots denote Gaussian expectation hypocenters.

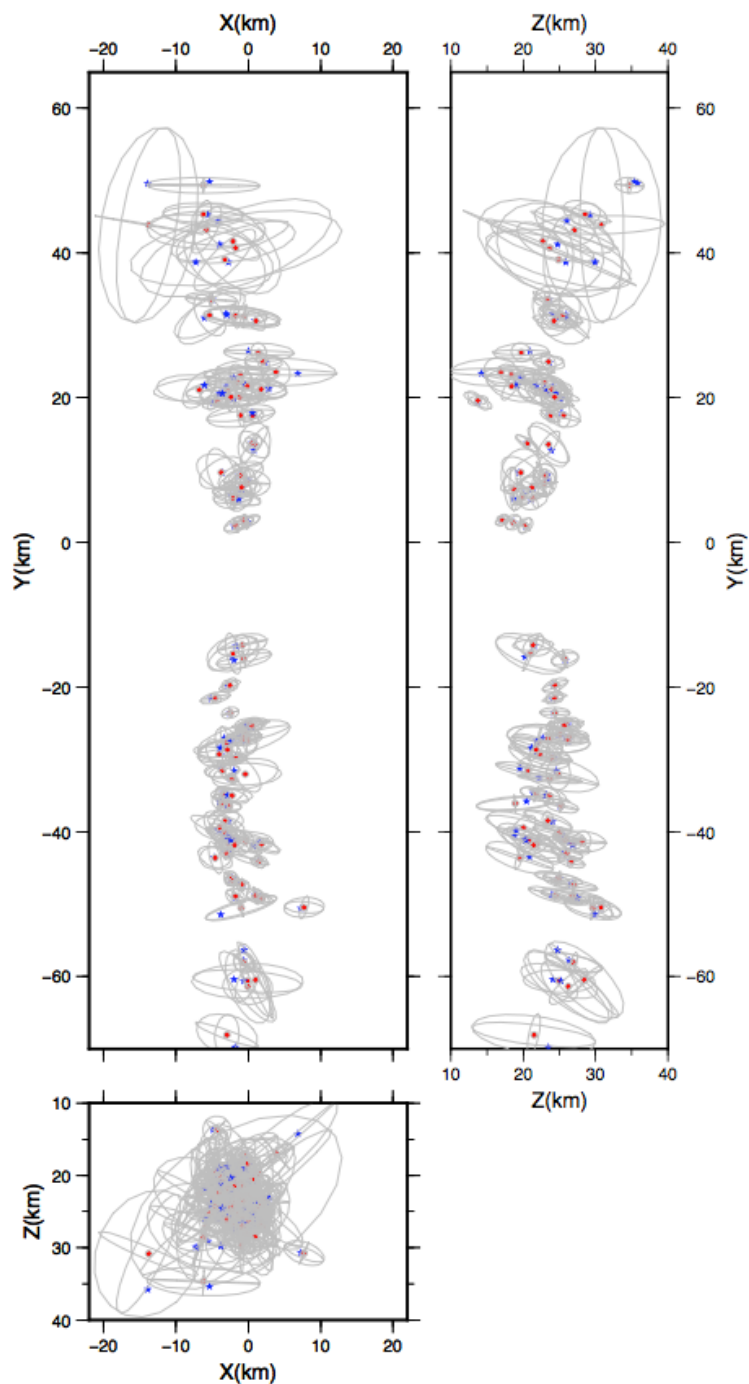


Figure 11. Comparison between NonLinLoc locations (black) and original locations (red, Shelly and Hardebeck, 2010). The surface trace of the SAF is shown in black line.

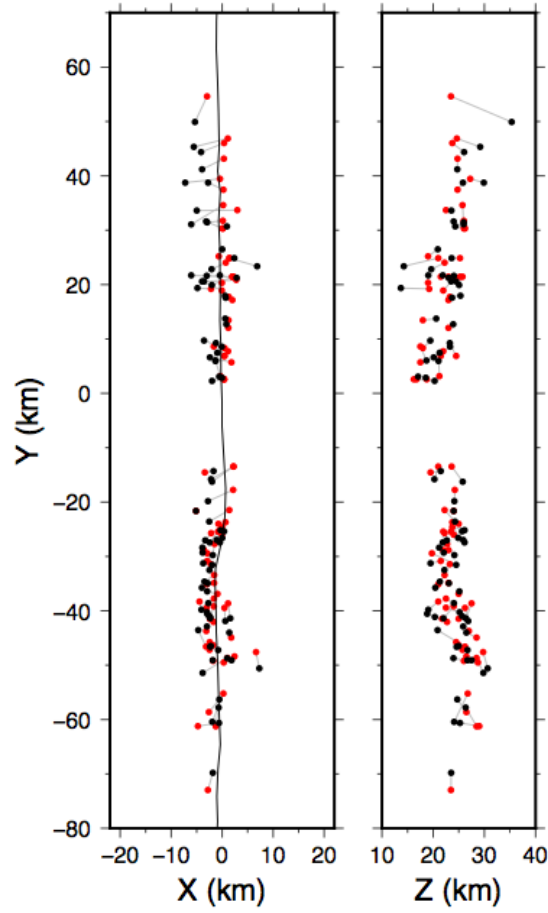




Figure S1. (Left) Tradeoff between norm of model and weighted travel-time misfit; (Right) Tradeoff between norm of model and unweighted travel-time misfit. The numbers show the smoothing weights and the arrow represents the chosen weight.

Table S1. Comparison between original locations (Shelly and Hardebeck, 2010), tomoDD locations, and NonLinLoc locations of 83 LFE families. Five LFE families have been deleted in tomoDD or NonLinLoc.